forum acusticum 2026
8-12 September · Graz, Austria

STRUCTURE-BORNE SOUND OF AN ELECTRIFIED POWERTRAIN - IDENTIFICATION OF LOAD CONDITION-BASED LOCAL MAXIMA

Lewin Weber-Karpinski[1], Erik W. Schneehagen[1], Thomas F. Geyer[1]

[1] *German Aerospace Center , Institute for Electrified Aero-Engines, Cottbus, Germany*

Abstract

The European Union is aiming for significant greenhouse gas reductions in aviation. In the course of this, electrified drive concepts are becoming increasingly important, resulting in new challenges with regard to the noise emission of electric machines. In order to gain a better understanding of the generation of noise, a coupled drive train consisting of two permanent magnet axial flux machines connected in series was investigated experimentally. The rotational speed and torque as well as the sound pressure level in the far field and surface velocity of the structure were measured at various stationary operating points and run-up scenarios using triaxial acceleration sensors, microphones and the information provided by the inverter. In order to draw conclusions about the excitation sources, spectral maxima of the measured quantities are compared with characteristic frequencies from theory. In addition, information from product data sheets, such as the number of pole pairs of the machine, is used as input parameters for this calculation. The method compares the spectra of different load-dependent test setups simulating a multitude of flight scenarios, which, considering the potential sources of the local maxima, may enable the design of low-noise concepts.

Keywords: *aircraft noise, electrified aero engines, vibration, structure-borne sound*

1. Introduction

Reducing anthropogenic greenhouse gas emissions is a key challenge in the transport sector [1]. Against the backdrop of the EU target of climate neutrality by 2050, technological innovations are also seen as a key lever for reducing emissions [2]. Electrified drive concepts are becoming increasingly important as they have the potential to reduce energy consumption, noise and pollutant emissions [3]. In this paper, the vibro-acoustic properties of such an electric drive train will be analysed. The basis is a data set from a measurement campaign together with the aircraft manufacturer Pipistrel, in which two coupled axial flux permanent magnet synchronous machines (AF-PMSM) were experimentally investigated [4]. The measurements include modal analysis of individual components, airborne sound pressure and torque measurements as well as operational vibration analyses of the entire system.

The aim is to identify the most critical excitation mechanisms that cause structure-borne noise depending on different load conditions or simulated flight scenarios. In order to speed up the evaluation of the extensive measurement data sets, an algorithm was used to automatically identify tonal structure-borne sound components. It is based on comparing calculations from the literature with the measurement results and filtering out the main contributors of the excitation spectrum. For this purpose, signal processing methods, the relevant excitation mechanisms and their spectral signatures are analysed. The different spectra of various test cases and physical quantities are then compared to one another with the aim to identify differences across those states.

2. Measurement Object

The investigated drive train seen in Figure 1 comprises two AFPMSM of type Emrax 268 MV+42% driven individually by two 2-level voltage source inverters.

Each motor can generate a maximum output power of 112 kW and 250 Nm of torque [5]. The maximum rotational speed is 4.500 rpm. However, the specific blade pitch limits the mission target speed at 2.300 rpm to avoid flow separation. The motors each have 10 pole pairs p and are cooled both by air and a water cooling circuit driven by a pump [5]. The inverters were devel-

Corresponding author: *lewin.weber-karpinski@dlr.de.*

Figure 1: View of drive train consisting of two coupled Emrax 268 MV+42% connected by stator cage.

oped in-house by Pipistrel. They run on three-phases with a switching frequency of 16 kHz. The modulation method used is space vector pulse width modulation (SVPWM). The calculated number of stator slots Q_s was found to be 60.

3. Setup

3.1. Experimental Modal Analysis

In order to differentiate between tonal components related to the rotational speed and the influence of structural properties of the motor, experimental modal analysis (EMA) was conducted on the accessible components of the drive train. For this purpose, the measured frequency response functions (FRF) were obtained using triaxial accelerometers. The FRFs describe the relationship between a defined excitation force and the structural response of the system in the frequency domain [6]. The natural frequencies of the system occur at the resonance points of these complex transfer functions [7]. The method used for the experimental determination of the modal parameters is Roving-Hammer. The method involves striking the structure successively with an impulse hammer at different excitation points while recording the structural response at defined measurement points on a grid representing the structure, where the response can be the displacement, velocity or acceleration of the surface.
In order to reduce random measurement deviations, each excitation point was struck three times, with the average of all three hits being calculated. To further decrease the influence of random noise, a multiple-input-multiple-output approach was chosen, i.e. the excitation of each point was recorded simultaneously at different points. The measurement of the signal in all three spatial dimensions enables the detection of coupled complex eigenmodes, consisting of a number of composite degrees of freedom [8].

3.2. Open Field Experiment

In order to investigate the vibration signal of the drive train, an operational deflection shape (ODS) analysis

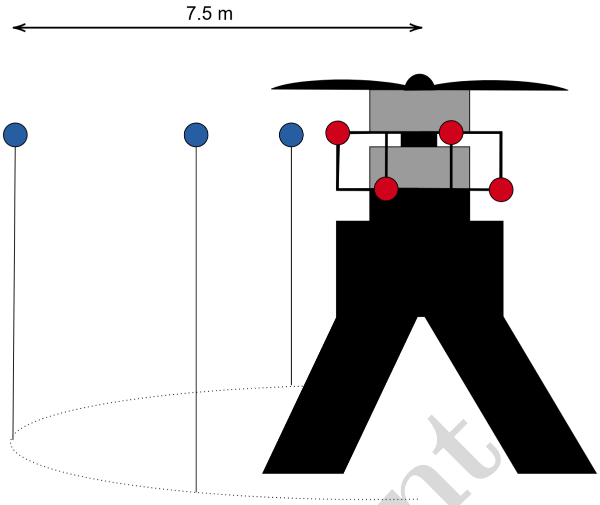

Figure 2: Schematic setup of the experiment with microphones (blue) in the motor plane and accelerometers (red) placed on the stator cage.

Table 1: Equipment used for the measurement campaign.

Type	Amount
Triaxial accelerometer, Kistler 8764B	4
Microphones, Microtech Gefell M380 MG	4
Impact hammer, PCB 086C03	1
Data acquisition unit Dewesoft Sirius X	2

was carried out to characterise the behaviour of the structure under real operating conditions [9]. The ODS thus provides the data basis for analysing the harmonic orders in relation to the shaft speed. For the measurements, the sensors had to be placed on the stator cage. Because of the out-runner configuration of the motor, measurements on the housing were not possible. In addition, as shown in Figure 2, the sound pressure was measured at three positions, each 7.5 m away and at an angle of 30 ° between the microphones. The motors and microphones were mounted at a height of 5 m. The quantities measured by Pipistrel, such as torque, were transmitted by a CAN bus. All signals were recorded through the same data acquisition system listed in Table 1 at a sampling frequency f_s of 50.000 Hz. Sensor signals of the same type were energetically averaged. The same applies for the spatial dimensions in radial coordinates of the accelerometers. This was done to obtain a single value for the vibrational data for demonstrative purposes. The reference values were chosen to be 10^{-6} m/s^2 for the acceleration, $2{\times}10^{-5}$ Pa for sound pressure and 1 Nm for torque.

3.3. Test Cases

The measurement addressed various flight scenarios for the coupled drive train. Table 2 shows the combi-

Table 2: Investigated flight scenarios with torque contribution of motor M1 and motor M2, load condition and corresponding scenario name.

M1	M2	load	name
50 %	50 %	propeller	m1-m2-p
50 %	50 %	no load	m1-m2-np
100 %	0 %	propeller	m1-0-p
100 %	0 %	no load	m1-0-np
0 %	100 %	propeller	0-m2-p
0 %	100 %	no load	0-m2-np

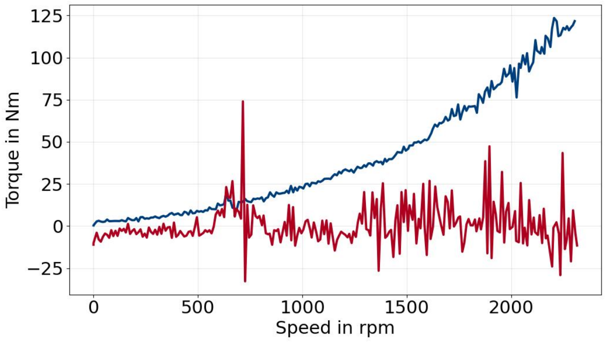

Figure 3: Torque over rotational speed for m1-m2-p (blue) and m1-m2-np (red).

nations in which the motors were tested. With the aim of simulating mission conditions, the target rotational speed was set to 2.300 rpm and consistent ramp-up speed across the measurements. The use of a single motor simulates the failure of the other one. Thus, the lack of torque provided by one motor has to be compensated for by the other one.
Figure 3 shows the difference in torque provided by one of the two motors during a run-up depending on the presence of a load. It can be seen that mounting the propeller stabilizes the torque, resulting in less ripple which would translate to lower levels of high-frequency noise. As a consequence, the amplitude of the torque ripple is small compared to the median, which in this case is around 125 Nm, corresponding to 30 kW of mechanical power. On the other hand, in the no-load case the amplitude of the ripple may be larger than the median rated torque. The median torque shown was calculated by averaging all samples within a span of 10 rpm. Given f_s and a ramp-up speed of 100 rpm/s, this results in 5.000 samples per data point in this figure. This downsampling was used just for visualization purposes.

4. Identification of Structure-Borne Sound-Inducing Components

The identification of potentially significant structure-borne sound-inducing frequency components is a three-step process. First, a number of theoretical motor orders compiled from theory is calculated. Then, along each order line within a search band the power spectral density (PSD) is averaged. Finally, only the calculated orders with the highest amplitude along their trajectory are depicted. Although not physically correct, the levels are averaged arithmetically. Knowing the most critical eigenfrequencies from the EMA, this approach was chosen to slightly mitigate the influence of resonances when compared to calculating the energetic sum along the spectral trajectory of a given order due to the logarithmic nature of the Decibel scale.

Table 3: Formulas used to calculate the respective frequencies of an integer slot wound electrical machine.

Source	Formula
Electrical frequency	$f_{\mathrm{elec}} = p f_{\mathrm{mech}}$
Blade passing frequency	$f_{\mathrm{BPF}} = b f_{\mathrm{mech}}$
Stator-stator force wave [10]	$f_{\mathrm{ss}} = 2\|\nu\| f_{\mathrm{elec}}$
Rotor-rotor force wave [10]	$f_{\mathrm{rr}} = 2\|\mu\| f_{\mathrm{elec}}$
Stator-rotor force wave [10]	$f_{\mathrm{sr}} = \|\nu + s\mu\| f_{\mathrm{elec}}$
Cogging torque [11]	$f_{\mathrm{cog}} = Q_{\mathrm{s}} l f_{\mathrm{mech}}$
Torque pulsation [11]	$f_{\mathrm{T}} = 2 n m_{\mathrm{ph}} f_{\mathrm{elec}}$
PWM [11]	$f_{\mathrm{pwm}} = n f_{\mathrm{c}} \pm o f_{\mathrm{elec}}$

Table 3 shows the formulas used for the identification process. Here, b is the number of propeller blades, n and o are ordinal numbers, s is $\in \{-1, +1\}$ and f_{c} is the carrier frequency of the pulse width modulation (PWM) of the inverter. The stator and rotor orders ν and μ can be calculated as

$$\nu = 1 \pm 6x, (x \in \mathbb{N}), \tag{1}$$

$$\mu = 1 \pm 2y, (y \in \mathbb{N}, y \neq 0). \tag{2}$$

Q_{s} can be calculated as

$$Q_{\mathrm{s}} = 2 p m_{\mathrm{ph}} q, \tag{3}$$

where m_{ph} represents the number of phases and q is the number of stator slots per pole per phase [12]. Without skewing, the winding factor k_ω can be described as

$$k_\omega = k_p k_d, \tag{4}$$

with k_p as the pitch factor and k_d as distribution factor. Assuming a k_ω of 1 given a high-torque density machine, k_p and k_d also become equal to 1 [13]. In a three phase motor, k_d can be expressed as [12]

$$k_d = \frac{\sin\frac{\pi}{6}}{q \sin\frac{\pi}{6q}}. \tag{5}$$

Equation (5) can then be solved for q to be used in Equation (3) to obtain the number of stator slots.
The parameter l can be described as

$$l = \frac{2p}{gcd(Q_s, 2p)}, \tag{6}$$

where gcd represents the greatest common divisor of stator slot number and pole number. Given the calculated Q_{s} in this specific machine, the frequency of the effects of cogging torque coincide with the slot

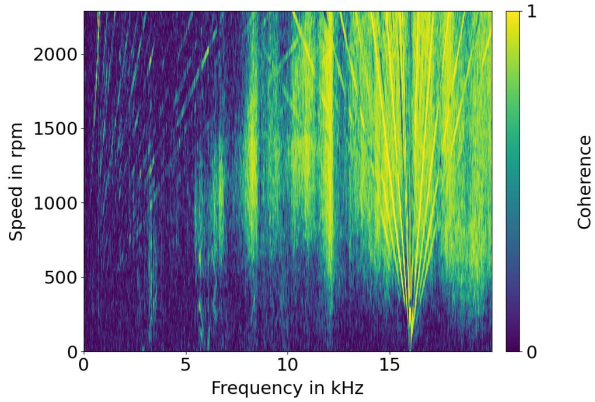

Figure 4: Coherence spectrogram between sound pressure and acceleration signal of m1-m2-np over rotational speed.

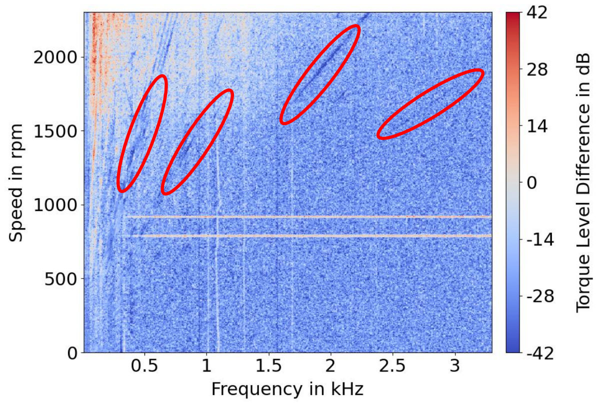

Figure 5: Difference of spectral torque level between m1-m2-p and m1-m2-np over rotational speed with 0 dB indicating congruent amplitudes between the signals. Red circles indicate relevant orders of the no-load case.

passing frequency.

5. Results

First, the coherence between the vibration signal and the sound pressure will be investigated. Therefore, m1-m2-np is shown in Figure 4, since the dominance of the f_{BPF} would strongly influence the visible correlation between the orders originating from the motor or inverter. High coherence can be observed in spectral areas where the motor housing is exited. The literature suggests that this is a highly radiating surface in axial flux machines [14]. This may be in part because the radiation coefficient is largely determined by the structure's ability to move air, which in turn is influenced by the effective area [15]. The deflection of the stator cage beams used as measurement positions therefore might be unfavourable. Consequently, the microphone signal will not be further investigated.
Next, Figure 5 shows the torque level difference between m1-m2-p and m1-m2-np, where negative levels indicate that more noise was generated for the configuration without a propeller mounted to the coupled motors. The higher broadband noise of the case without load can be explained by the same effect that was observed in Figure 3, where these frequencies occurred as ripple in the time domain. Also, higher amplitudes at multiples of f_{BPF} in the low frequency range of the reference signal were to be expected since only the load case had a propeller attached. However, the 20^{th}, 40^{th}, 60^{th} and 120^{th} motor order (marked in the plot) as well as some of their side bands seem to be emphasized without load, with the side bands being dependant on $\pm f_{\mathrm{mech}}$.
In Figure 6 it is shown that apart from the vertical lines representing the influence of low eigenfrequencies (especially the eigenmodes of the housing of the motor), the coherence between the torque and the acceleration signal in m1-m2-np is highest at those mentioned orders. Thus, the torque, as a result of the tangential forces in the air gap, shares overtones of the same time orders as the vibration signal, which mainly originates from the radial forces [10]. This

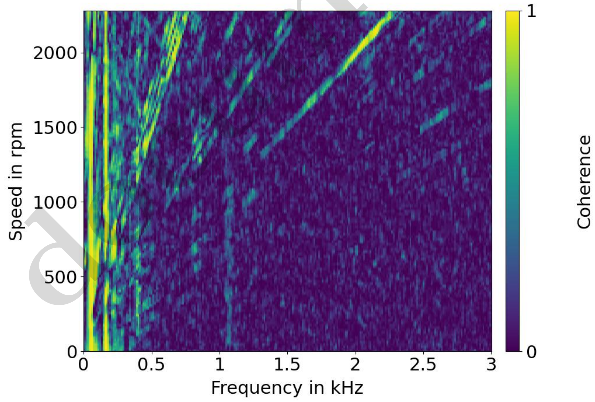

Figure 6: Coherence spectrogram between torque and acceleration signal of m1-m2-np over rotational speed.

hints towards both signals originating from the same geometrical property. It is suspected that the motor's specific stator slot - pole pair combination being modulated by the rotational speed is the main parameter influencing this ripple. However, the 60^{th} and 120^{th} order may be attributed to the effects of cogging torque according to Table 3.
Due to the high coherence under no-load conditions, the vibration signal can be analysed using the identification method proposed in Section 4 in order to determine spectral components. Also, it provides more details due to the higher resolution of the sensor type and thus allows to find further, less dominant sources. Therefore, Figure 7 shows the 20 motor orders of the vibration signal of m1-m2-np with the highest average level (excluding the PWM spectrum) as well as their possible causes. The prominent torque ripple indicated earlier can be traced to the combined effects of the stator, rotor and stator slot-modulated rotor force waves, with all of them coinciding at the 20^{th} order. The 120^{th} order identified in Figure 6 can be linked to cogging torque and torque pulsation frequencies.

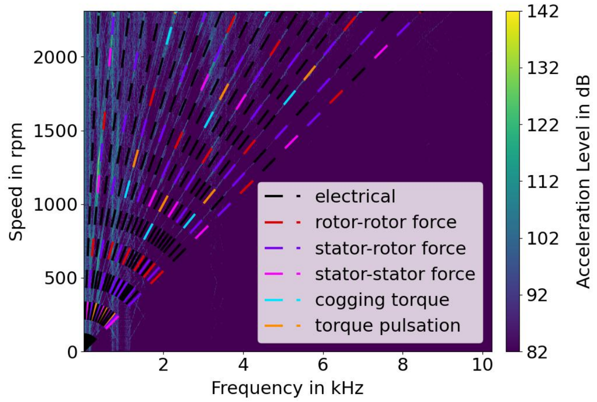

Figure 7: Identification of possible excitation mechanisms of the 20 vibrational orders of highest averaged level along each order in m1-m2-np.

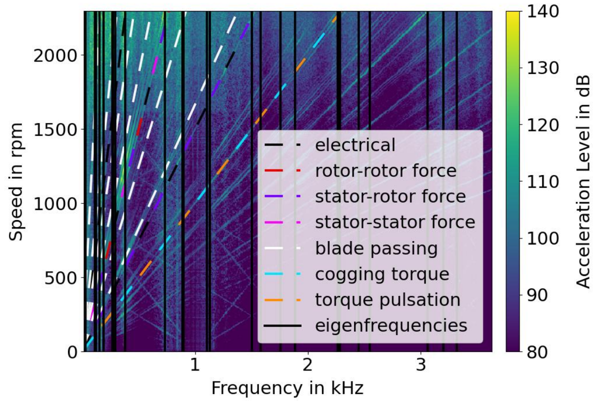

Figure 8: Spatially averaged acceleration level spectrogram with measured eigenfrequencies of the drive train in vertical direction in black. Dashed lines represent the 10 orders with highest time averaged levels and lowest for m1-m2-p.

The presence of the 20^{th} order is likely to be enhanced by an l of 1 and the combination of the specific number of stator slots and electrical phases, resulting in overtones of both effects occurring at multiples of 60. Although coincidence of multiple excitation mechanisms may play a role, Figure 7 reveals that higher time orders of the stator slot-modulated rotor force wave tend to create time orders with a generally high vibrational amplitude compared to other sources. The 60^{th} mechanical order identified earlier is also part of this frequency family. It's strong presence may be related to the fact that when calculating f_{sr} and dividing it by the electrical frequency, a large number of combinations (ν, μ) fall onto this third order force wave. Apart from the visible resonances with low eigenfrequencies, lower order harmonics carrying more energy than higher ones can be observed. This is to be expected since the amplitude of harmonics of the exciting field waves decreases by a factor of k_{ω}/ν [11]. In what follows, the scenario m1-m2-p will be shown to investigate the effects in place during mission conditions. In Figure 8, the results are shown together with the measured eigenfrequencies. For demonstrative purposes, only the lowest order harmonic among those coinciding will be shown. This is, unless different sources share the same multiple. Additionally, the blade passing frequency was added to the identification method for the acceleration signal since the propeller was attached during these run ups. It can be seen that at target rotational speed the electrical frequency, 1^{st}, 2^{nd} and 5^{th} f_{BPF} as well as the 1^{st} f_{rr} are in resonance with eigenfrequencies of the stator cage and motor casing, resulting in high acceleration levels. In what follows, the difference between m1-m2-np and 0-m2-np will be investigated as an example for the scenario simulating one failing motor.

In Figure 9, the difference of the acceleration level spectra is presented. It shows the five orders of each highest and lowest absolute level differences. For orders with coinciding sources, again only the lowest

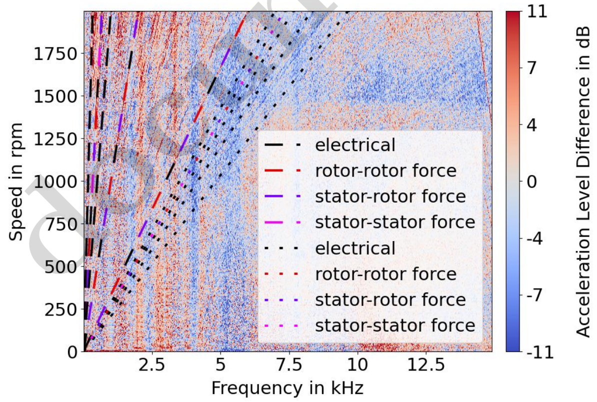

Figure 9: Spectral acceleration level difference between m1-m2-np and 0-m2-np over rotational speed with 0 dB indicating congruent amplitudes between the signals as well as dashed lines representing highest and dotted lines lowest amplitude orders.

multiple was plotted. Due to the negative level of orders in the range between 7 kHz to 8 kHz as well as 16 kHz to 18 kHz at 2.000 rpm, it can be stated that the single motor case amplifies those orders compared to m1-m2-np. Also, the lower orders as well as the PWM spectrum appear stronger when coupled than in single motor use. The presence of the PWM spectrum could be explained by the fact that each motor was driven by a separate inverter and in 0-m2-np, only one was engaged. For the higher amplitude of high orders in 0-m2-np mostly multiples of f_{elec} are observed. While unclear as to why this occurs, it might play a role which single motor is exciting the structure, since this effect could not be found when investigating m1-0-np.

In Figure 9, the engine that is further from the drive train's mounting provided the torque. When thinking of the shaft as a cantilever beam, the vibrational signal may differ along with the distance to the mounting and the number of excitation sources, e.g. motors in series.

6. Conclusion and Outlook

A drive train consisting of two coupled AFPMSM was investigated with the aim to identify possible sources of vibro-acoustic excitation in an aircraft. Expected frequencies from literature could be found in the measured acceleration spectra. With respect to the known spectral location of the measured eigenfrequencies, the arithmetic averaging of the level of the harmonic orders was used to show tendencies of which orders carry the most energy. When combined with the analysis of the torque signal it could be derived that the force wave of the stator slot-modulated rotor magnetic field plays a significant role especially at higher speeds, when the influence of the windings, be it by higher currents needed or the rising counter-electromotive force, becomes more relevant. The proposed method is helpful in obtaining an overview of the most relevant acting forces. The foundation of frequency families used to match the harmonic orders seems to be working. For the investigated drive train the specific stator slot and pole combination turns out to be unfavourable regarding the alignment of the many exciting mechanisms at the 20^{th} order since it dominates the signal. This effect is amplified by the fact that a motor casing's eigenmode is in resonance with this order at target rotational speed. Extensions to the current model, such as continuos bearing fault detection frequencies, may be added to identify further orders. Also, side bands of certain orders are currently neglected. In the future, the addition of modulation frequencies of the force waves by $\pm f_{\text{mech}}$ or $\pm f_{\text{elec}}$ may be considered if strong evidence of these side bands is found.

7. Acknowledgments

The authors thank the staff of Pipistrel for the opportunity to perform these measurements in the framework of the SyneLa project.

References

[1] Directorate-General for Mobility and Transport (European Commission) and Directorate-General for Research and Innovation (European Commission), "Flightpath 2050: Europe's vision for aviation: Maintaining global leadership and serving society's needs," European Commission, Luxembourg, Tech. Rep., 2011.

[2] European Commission, Directorate-General for Communication. "Indicating the way forward for sustainable European aviation," Accessed: Feb. 19, 2026. [Online]. Available: https://commission.europa.eu/news-and-media/news/indicating-way-forward-sustainable-european-aviation-2025-01-14_en

[3] Deutsches Zentrum für Luft- und Raumfahrt (DLR). "Die Zukunft fliegt elektrisch," Accessed: Feb. 19, 2026. [Online]. Available: https://www.dlr.de/de/forschung-und-transfer/themen/klimavertraegliches-fliegen/die-zukunft-fliegt-elektrisch

[4] PIPISTREL. "Pipistrel," Accessed: Apr. 15, 2026. [Online]. Available: https://www.pipistrel-aircraft.com/

[5] EMRAX d.o.o. "Emrax 268," Accessed: Apr. 13, 2026. [Online]. Available: https://emrax.com/e-motors/emrax-268/

[6] T. Irvine. "An Introduction to Frequency Response Functions," Accessed: Aug. 13, 2025. [Online]. Available: https://www.vibrationdata.com/tutorials_alt/frf.pdf

[7] T. L. Schmitz and K. S. Smith, *Single Degree of Freedom Forced Vibration*, 2nd ed. Cham, Switzerland: Springer, 2021, pp. 89–132. DOI: 10.1007/978-3-030-52344-2_3

[8] L. Weber-Karpinski, "Körperschallinduzierende Komponenten eines elektrifizierten Luftfahrtantriebes," M.S. thesis, Hochschule Mittweida / Hochschule München, Mar. 2026.

[9] J. Baqersad and D. D. Maio, Eds., *Computer Vision & Laser Vibrometry, Volume 6: Proceedings of the 41st IMAC, A Conference and Exposition on Structural Dynamics 2023*, Conference Proceedings of the Society for Experimental Mechanics Series, Cham, Switzerland: Springer Nature Switzerland AG, 2024. DOI: 10.1007/978-3-031-34910-2

[10] J. F. Gieras, C. Wang, and J. C. Lai, *Noise of Polyphase Electric Motors*. Boca Raton: CRC Press, 2006.

[11] A. Binder, *Elektrische Maschinen und Antriebe: Grundlagen, Betriebsverhalten*, 2nd ed. Berlin, Heidelberg: Springer Vieweg, 2018.

[12] J. Pyrhönen, T. Jokinen, and V. Hrabovcová, *Design of Rotating Electrical Machines*. Chichester, United Kingdom: John Wiley & Sons, Ltd., 2008.

[13] Y. Sun, W. Zhao, J. Ji, J. Zheng, and Y. Cheng, "Torque improvement in dual m-phase permanent-magnet machines by phase shift for electric ship applications," *IEEE Transactions on Vehicular Technology*, vol. 69, no. 9, pp. 9601–9612, Sep. 2020. DOI: 10.1109/TVT.2020.3004161

[14] P. Kotter, C. Köpf, J. Berkemer, O. Zirn, and K. Wegener, "Acoustic characterization of electrical motors based on magnetomechanical and drive-system issues," in *18. Internationales Stuttgarter Symposium: Automobil- und Motorentechnik*, M. Bargende, H.-C. Reuss, and J. Wiedemann, Eds., Wiesbaden: Springer Vieweg, 2018, pp. 91–109.

[15] L. Cremer, M. Heckl, and B. A. T. Petersson, *Sound Radiation from Structures*, 3rd ed. Berlin, Heidelberg: Springer, 2005, pp. 449–535. DOI: 10.1007/3-540-26514-7_7